De la Asunción-Nadal, V. et al. (2023) 'Transition metal dichalcogenide micromotors with programmable photophoretic swarming motion', Journal of materials chemistry. A, Materials for energy and sustainability, 11(3), pp. 1239–1245.

Available at https://doi.org/10.1039/d2ta07792b

ARTICLE

Transition metal dichalcogenide micromotors with programmable photophoretic swarming motion

Received 00th January 20xx,
Accepted 00th January 20xx

DOI: 10.1039/x0xx00000x

Víctor de la Asunción-Nadal,[a] Daniel Rojas,[a] Beatriz Jurado-Sánchez,*[a,b] and Alberto Escarpa*[a,b]

Herein we report the light-triggered photophoretic motion of WS_2 micromotors. The micromotors are prepared by liquid-phase exfoliation of pristine WS_2 in water, resulting in a layered material with high photoconversion capability. Under electromagnetic irradiation in the UV or VIS range, the micromotors exhibit a positive photophoretic motion and swarming-like schooling behavior. The light-induced heating of the prepared micromotors is studied and computational fluid dynamics simulations are considered to characterize the photophoretic propulsion mechanism. The novel micromotors described here are able of performing a collective motion without the need for surfactants, fuels, or other reagents, reaching velocities of up to 6000 μm s^{-1}. To date, this represents the fastest light-driven micromotor platform, paving the way for novel cutting-edge applications.

Introduction

Micromotors are micro sized objects capable of performing complex tasks in miniaturized environments with a myriad of applications ranging from microsurgery to environmental remediation or analytical sensing.[1-7] An interesting feature of self-propelled micromotors is the ability to work cooperatively as a swarm, leading to accelerated and improved fluid mixing.[8-10] The first exploited driving force to promote a cooperative micromotor motion are chemical gradients. For example, doxorubicin-loaded stomatocyte micromotors either modified with platinum nanoparticles[11] or catalase[12] exhibit chemotaxis towards H_2O_2 gradients, which are generated by cancerous cells. Polymer microspheres coated with catalytic Pd nanoparticles can sense and direct its motion towards OH^- gradients.[13] Yet, all the above-mentioned configurations rely on the use of inputs of relatively toxic reagents, which can limit certain applications or restrict them to certain environments. Consequently, external energy inputs like magnetic fields, ultrasounds or light are promising for further applications.

Magnetic fields were used to induce the motion of micromotors for the creation of swarms by tuning the rotation and strength of applied magnetic fields, either in magnetically propelled helices,[14] supramolecular micromotors [15] or glucose fueled Janus micromotors loaded with magnetic nanoparticles.[16] Similarly, acoustic (ultrasound) driven Au nanowires can accumulate in the pressure nodes of acoustic fields for enhanced Raman detection of miRNA in serum samples.[17, 18] Electromagnetic (light) fields are one of the most versatile external sources to promote micromotor swarming due to their low cost, precise control, and biocompatibility.[19] Photocatalytic micromotors are synthesized using semiconductor materials that possess electronic structures available for the interaction of electrons with electromagnetic radiation, generating electron-hole pairs to trigger the propulsion; either by the electrophoretic or photothermal mechanisms. Indeed, and specifically in semiconductors, the relaxation of electron-hole pairs can occur non-radiatively by the generation of phonons that increase the lattice temperature and trigger the photothermal effect. Alternatively, the reaction of free electrons and positive holes with surrounding molecules triggering a diffusiophoretic motion.[20] Photoactive TiO_2 micromotors can form swarms by irradiation with UV light in a fluid-filled microchamber due to a mix of propulsion mechanism, including diffusioosmotic swarming and photothermal effects.[21] TiO_2-OH micromotors display schooling and cooperative behavior under UV light irradiation due to nonelectrolyte diffusiophoretic interactions, exhibiting also negative phototaxis.[22] Platinum nanoparticle micromotors decorated with carbon nitride can experience negative and positive phototaxis upon UV light irradiation, due to the generation of proton and hydroxyl radicals in an electrophoretic mechanism.[23] AgNW@SiO_2 core–shell nanomotors rapidly aggregate after application of UV light for Raman sensing following a similar principle.[24] MoS_2 colloidal micromotors can move into a swarm due to a dominant self-diffusiophoretic effect, exhibiting a phototactic motion for the creation of dynamic shapes.[25] Yet, such strategies cannot be used in high ionic strength media, which hampers future practical applications.

Some materials such as Au, graphene, Fe_3O_4, etc. can absorb light to convert it into local heat on their surfaces, producing a temperature gradient across irradiated and unirradiated areas, leading to a convective flow and hydrodynamic drag that generates a collective behavior. This process is known as photophoresis or light-induced motion. According to this principle, particles can display motion, either in the same or in the opposite direction of the radiation source, following different paths such as linear or

[a] Department of Analytical Chemistry, Physical Chemistry and Chemical Engineering, University of Alcala, Alcala de Henares, Madrid, E-28871, Spain. E-mail: beatriz. jurado@uah.es; alberto.escarpa@uah.es; Tel: +34 91 8854995
[b] Chemical Research Institute "Andres M. del Rio", University of Alcala, Alcala de Henares, Madrid, E-28871, Spain

† Electronic Supplementary Information (ESI) available: Experimental, suppotign data, supporting figures and supporting videos. See DOI: 10.1039/x0xx00000x

helicoidal. This motion is due to the different mobility of the surrounding solvent molecules.[26, 27] For example, NIR light have been used to control the swarming and collective migration of TiO_2/Pt, SiO_2/Pt, TiO_2 or ZnO micromotors by light induced convection flows.[28] Polymer microparticles have been modified with Fe_3O_4 as thermoresponsive material. The photogenerated heat of the nanoparticles decrease the density of the irradiated solution, thus rendering a convective flow and hydrodynamic drag to promote the schooling and swarming behavior of the particles.[29] Transition metal dichalcogenides (TMD) are 2D materials applied in different fields due to their unique electrical, [30] electronic, [31] and optical properties.[32] These materials are defined as atomically thin semiconductors with a MX_2 structure, being M a transition metal (W, Mo, Ta, etc.) layer sandwiched between two chalcogenide (S, Se, Te, etc.) layers. The unique optical properties of these materials emerge while scaling down towards few-layered materials due to quantum confinement transitioning from indirect to direct bandgaps and high surface-to-mass ratio [33, 34] thus being able to fine-tune these optical features. As a result of their semiconducting nature, TMDs can absorb photons with an energy equal or larger to that of their bandgap and thus, heat up under electromagnetic irradiation. [35] These properties have been explored by our research group for the synthesis of catalytic WS_2/Pt tubular micromotors, which are able to respond to NIR light, generating reactive oxygen species (ROS) for pollutant degradation. However, the use of the photothermal properties of WS_2 microparticles as light-driven micromotor engines remains unexplored.[36] Intrigued by the light-responsive abilities of TMDs and the ability to interact with light and transduce it into thermal energy, herein we explore the light-induced swarming effect and behavior of colloidal WS_2 as micromotor under UV and VIS light irradiation due to the photophoretic effect.

Results and discussion

Fig. 1 illustrates the concept of the multiwavelength-responsive WS_2 micromotors. As can be seen in the illustrations and in the time-lapse images (taken from **Video S1**), the micromotors experience a fast-schooling behavior, forming a swarm that can be assembled-disassembled by turning the light ON or OFF, reaching maximum speeds of over ~6000 µm s^{-1}, being the fastest reported to date (see **Table S1** for a comparison with other light driven micromotors reported to date). The recorded speeds represent a 20-fold increase compared to the fastest speed previously reported for photothermal micromotors, which to date ranged from 25 to 270 µm $s.^{-1}$ [28, 29, 37] Also, the speed of our micromotors is higher than that reported for other swarming micromotors such photocatalytic powered hematite/Pt micromotors (32 µm s^{-1} in 5 % H_2O_2) [38]; $BiVO_4$ micromotors (6 µm s^{-1} in 2 % H_2O_2)[39] or ZnO/Ag micromotors (5 µm s^{-1} in 2 % H_2O_2).[40] Regarding diffusiophoretic micromotors triggered by UV light, speeds of up to 23 µm s^{-1} have been reported for swarming carbon nitride micromotors.[41] Thermoresponsive NIR triggered gold-copper micromotors reach speeds of up to 40 µm $s.^{-1}$ [42] In all these micromotor-based approaches, speeds are from 150 to 1000 times lower than the reported in this article. It should be noticed here that in the previously mentioned articles, the micromotors can be triggered upon the action of UV light, while our micromotors can move in the full UV-Vis light spectra.

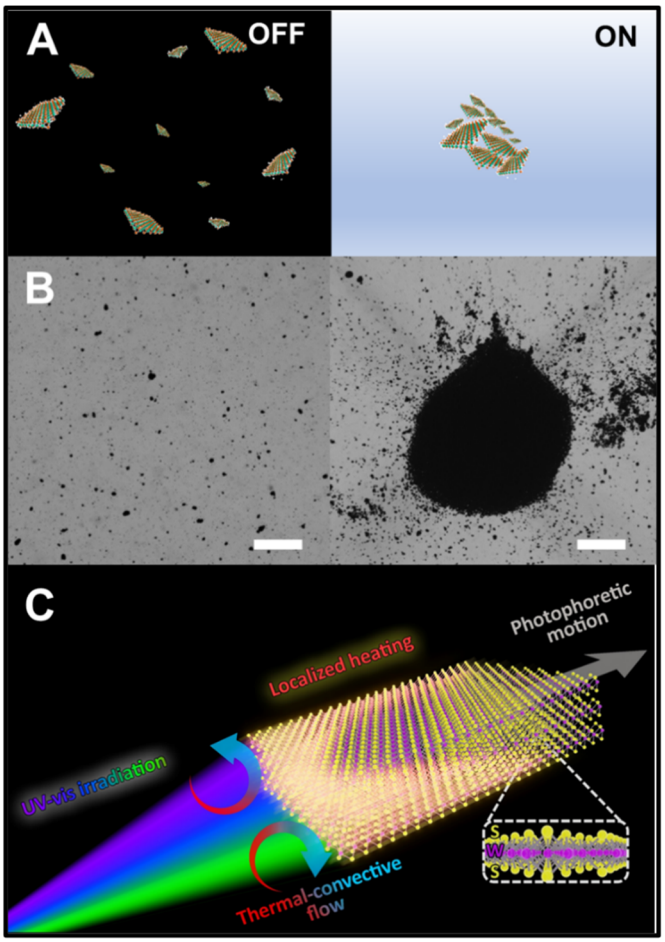

Fig 1. Photophoretic WS_2 micromotors with swarming motion. A) Schematic of the concept prior (OFF) and after light irradiation (ON) and B) corresponding time-lapse images (30 seconds) of the motion of WS_2 micromotors under VIS light (550 nm) irradiation. C) Schematic of the proposed propulsion mechanism. Scale bars, 50 µm.

The micromotors were prepared by liquid-phase exfoliation of pristine WS_2 in water. The resulting particles are light-responsive and able to move without further cleaning or size purification steps. Different incident radiation wavelengths were used: UV= 385 nm, blue = 475 nm, green = 550 nm, and red = 621 nm. The photon energy absorbed by the micromotors generates excited charge carriers and holes for radical generation due to the reaction with the aqueous media. More importantly, as previous reports indicate, WS_2 displays good photothermal conversion capabilities.[43] Dissipation of this energy induce a thermal effect, heating up the surrounding media. This generates a hydrodynamic flow, and consequently, a self-thermophoretic motion, which promotes the cooperative schooling behavior of the micromotors (see the proposed propulsion mechanism in the supporting information). To get further insight into the motion mechanism, judicious studies of the micromotor morphology and motion in different media were performed, along with convenient numerical simulations.

Fig. 2 illustrates the morphological characterization of the WS_2 micromotors by scanning and transmission electron microscopy (SEM and TEM, respectively), Raman and atomic force microscopy (AFM). The SEM (**Fig. 2A**) and TEM (**Fig. 2B**) micrographs illustrate irregularly shaped particles. The absence of major impurities was assessed by electron-dispersive X-ray spectroscopy (EDX, **Fig. 2A**). Additionally, the size of 15 micromotors was measured by means of TEM imaging, obtaining an average micromotor size of 800 ± 300 nm. Furthermore, close TEM inspection of the micromotors' morphology revealed the presence of crystallites with an average size of 50 ± 18 nm, revealing the polycrystalline nature of the photophoretic WS_2 micromotors. AFM of an individual WS_2 particle (see **Fig. 2B, b**) was also recorded to get insights into mean geometrical features, which are of great importance to design a 3D model for fluid dynamics simulations to understand the proposed propulsion mechanism. The Raman spectrum of the WS_2 particles is depicted in **Fig. 2B, c**, and displays two main bands centred at 350 cm^{-1} and 420 $cm.^{-1}$ The first band corresponds to the in-plane phonon mode $E_{2g}{}^1$, whilst the second is attributed to the out-of-plane A_{1g} phonon mode. [44, 45] These bands and their relationships will be further studied to analyse the structural interaction of these materials with light. **Fig. 2C** and the corresponding size distribution plot of **Fig. 2D** shows the representative mean geometrical features of WS_2 micromotors, showing irregular flakes in shape and a mean thickness of 300 nm. The interaction of WS_2 with electromagnetic radiation was studied by means oft UV-vis absorption spectra and related TAUC plots (see **Fig. S1**). The calculated optical bandgap is 2.25 eV. The incident photon energies of the different electromagnetic radiations used for promoting the motion of the micromotors are equal to 3.2 eV for UV, 2.6 eV for blue, 2.3 eV for green, and 2.0 for red light respectively.

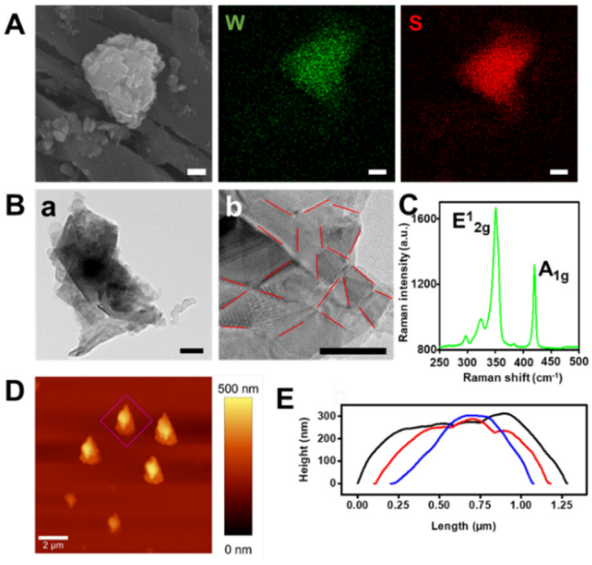

Fig. 2. Characterization of the WS_2 microparticles. A) SEM and EDX mapping showing the element distribution. Scale bars, 250 nm. B) TEM of a (a) single micromotor and (b) amplification on a micromotor with the crystallite separation marked with red lines. Scale bars, 100 nm. C) Raman spectra. D) Topographic AFM image showing the height and morphology of a representative micromotor and E) corresponding length and height profile of several particles.

As photophoretic micromotors can be propelled by different mechanisms (electrophoresis, self-thermophoresis or photophoresis), we studied the motion performance of the WS_2 micromotors in terms of mean particle velocity and composition of the media (water and non-ionizable solvent). The speeds of different WS_2 micromotors were recorded when exposed to UV (128.4 mW), blue (82.0 mW), green (105.4 mW), and red (117.0 mW) light. The results are shown in **Fig. 3A**, along with the corresponding tracking lines. First, we studied the role of photocatalyzed species in a possible self-electrophoretic motion of the micromotors. **Fig. S2** illustrates the amperometric signal of solutions containing the WS_2 micromotors and phosphate buffer saline (PBS) solutions while irradiated in subsequent OFF-ON cycles of illumination (for more details, see the experimental section). A sharp increase in the amperometric signal is noted after light irradiation, with an equal decrease after turning the light off. Alternatively, negligible signal variations are observed in PBS solution in the absence of micromotors, indicating the production of ROS ($^{\cdot}OH$, $O_2^{\cdot-}$, $^1O_2$, etc) from the light-activated WS_2 micromotors. [46] To check a potential leading role of ROS generation in the driving mechanism, we recorded the micromotors' motion in water and in dimethylformamide (DMF) as a non-ionizable organic solvent. The micromotors were tracked in both media and their velocities compared. As can be seen in the speed plot of **Fig. 3** and **Fig. S3**, the WS_2 micromotors show efficient propulsion in both media. Such results reveal that the electrophoretic motion mechanism is not responsible for the micromotor motion. In other words, the TMDs micromotors show a light-dependent movement due to photothermal effects. The propulsion can be due to the uneven heating of the micromotors due to the illumination with the light source (photophoresis), with subsequent heat release and thermal convection that generate a hydrodynamic flow around the micromotors, or the establishment of density gradients. [29, 47-50] The different motion patterns of **Fig. 3B** were studied in Python simulations (see **Fig. 3C**, for further details please refer to the Supporting information, **Fig. S4**) to differentiate the distinct motion mechanisms. As can be seen, the WS_2 micromotors move in a convective-like motion from the non-irradiated region to the irradiated area. It is also possible to guide them to a focusing point along the surface, where accumulation is induced. This observation is in line with a positive photophoretic mechanism.[51, 52] Finally, as observed in **Video S2**, under the same irradiation, less photoactive materials such as graphene oxide flakes prepared under the same conditions do not show any phototactic behaviour. Also, convective motion is not observed as proven by the absence of motion of suspended tracer polystyrene beads. This eliminates the possibility of a collective photothermal effect. Hence, the photophoretic mechanism is identified as the main contribution to the observed, fast micromotor motion. In addition, photophoretic Fe_2O_3@WS_2 magnetic micromotors (see Experimental Section) also exhibited swarm-like collective behaviour with similar speed profiles, which allows expanding its applications (see **Video S3**). Finally, a control experiment in an enclosed environment was carried out (see **Video S4**). In such conditions, the micromotors experienced similar light-driven behaviour. This discards a possible leading role of the

Marangoni effect through the liquid-air interface in the motion of the reported photophoretic micromotors.

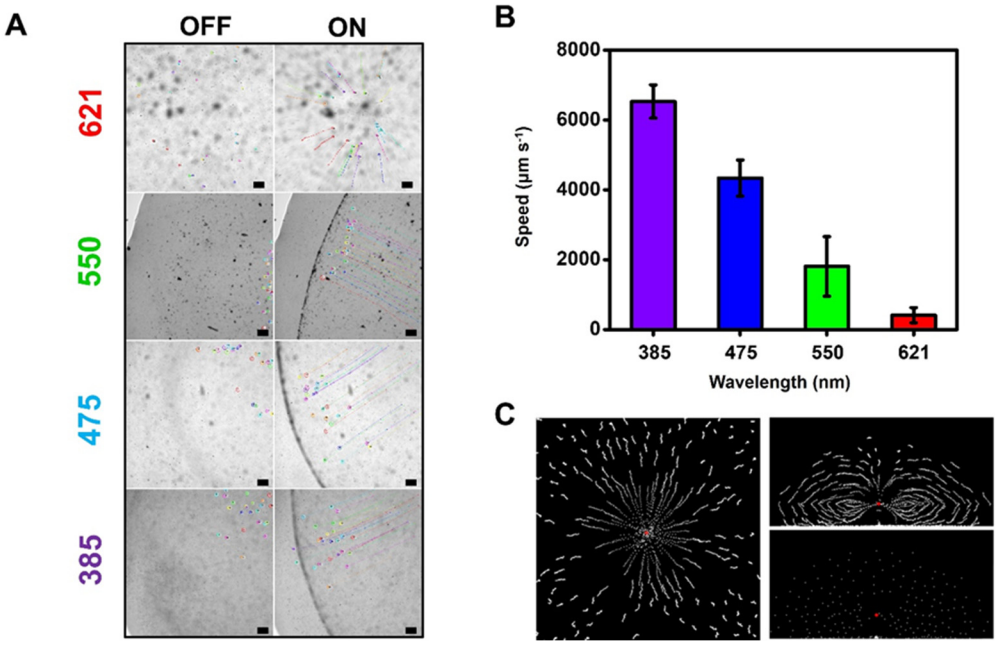

Fig. 3. A) Time lapse-images (taken from **Video S2**) of the OFF-ON motion and particle trajectories of WS_2 micromotors under UV, blue, green, and red light irradiation B) Speeds of the micromotors under different light irradiation wavelengths in water. C) Python demonstration the motion of micromotors in the XY plane in time-lapse mode (left) and in the XZ plane, time-lapse (right-top) and instant picture (right-bottom). Scale bars, 50 μm.

As can be observed in **Fig. 4**, the micromotors display two differentiated behaviours. Firstly, in the fluid body, micromotors can engage a fast convective-like motion. Alternatively, the micromotors close to the substrate can "crawl" towards the focal point. Micromotors can perform a collective motion into swarms. Interestingly, the swarm's size can reach a plateau that is dependent on the irradiation time as shown in **Fig. 4A**. We hypothesize that the size of the swarms may be related to the speed, as higher speed micromotors are able to overcome the interparticle repulsion forces more efficiently and pack the micromotors in the swarm more efficiently. It is worth noting that both motion regimes are of great interest for different applications. To fully understand these processes, the main forces involved in the motion of the micromotors must be taken into consideration. **Fig. S4** depicts a schematic representation of the main forces involved in the motion of the WS_2 light-driven micromotors. Firstly, as seen in **Fig. 4B**, we assume that micromotors migrate to the focal point by a photophoretic mechanism, while particle-substrate interactions keep the closest particles to the substrate from swimming up from the swarm. Next, when the light irradiation is switched off, the Brownian motion and electrostatic repulsion between micromotors take over, generating a fast growth of the area covered by the micromotors as they diffuse away from the original focal point. Finally, when light is irradiated in a different point, the micromotors can move as a swarm to the new focal point, clearing the original spot. Remarkably, due to the repulsive interactions between micromotors, the individuality of each micromotor is preserved, allowing for further disengagement from the swarm and self-photophoresis after a new irradiation is set. This also allows for the selective anchoring and removal after the desired operation.

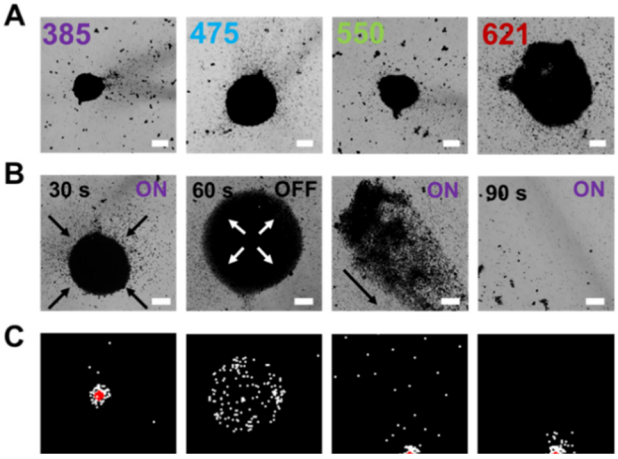

Fig. 4. A) WS_2 micromotor's swarming ability under 385 nm, 475 nm, 550 nm, and 621 nm irradiation. B) Time lapse images of WS_2 micromotors (from left to right) after irradiating for 30 seconds a fixed spot, not irradiating for 30 seconds, irradiation of a different spot, and the first spot after 30 seconds of irradiation in the second spot (taken from **Video S1**). Scale bars, 50 μm.

Light-induced heating of TMDs has been previously reported, [53] nonetheless, to assess the magnitude of the heating in our system, the Raman spectra of WS_2 particles were recorded at low irradiation power (0.05 mW) at different temperatures (50, 100, 150, 200, 250, 300, 350 and 400 ºC) for 10 s. The temperatures were stabilized for 20 minutes before each measurement. To this end, a thermostatic cell coupled to a Raman confocal microscope was used. After irradiation, the Raman spectra was taken to get some insights in the Raman shifts (see **Fig. 5A** and the corresponding plot of **Fig. 5B**). As can be seen, the characteristic 418 cm^{-1} band shifts to lower wavenumbers when the temperature increases. Additionally, at higher temperatures, the intensity ratio of the bandgaps at 352 and 418 nm^{-1} also increases.

Next, the Raman spectra of WS_2 micromotors was recorded while irradiated at higher power (0.50 mW). As can be seen in **Fig. 5C**, the local temperature increases up to 500 ºC during irradiation, with a shift in the 418 nm^{-1} band.g This supports the heating and subsequent heat exchange from the micromotors, generating the photophoretic effect. The results show a local temperature increase in the range of up to 500 ºC in static conditions. Such data indicates that the micromotors are indeed heated mainly in the middle (center regions) as seen in **Fig. S5**, whereas heat is dissipated in the edges. [54] Additionally, as seen in **Fig. 5C**, up to 4 irradiation cycles were performed. As observed, a temperature increase is observed in each cycle, nonetheless the increase is less substantial in each iteration. Due to the relatively low reported thermal stability of WS_2, after each heating-cooling cycle, physicochemical or structural changes may undergo and affect the photoconversion capacity of the studied microflakes.[55]

Furthermore, the bulk temperature of different dispersions containing WS_2 micromotors was measured at the studied wavelengths as shown in **Fig. 5D**. As seen in the figure, the heat flow between the particles and the surrounding fluid allows for the dissipation of the photothermal localized temperature increase, reaching less than 40 ºC in all cases. Interestingly, the stationary temperature is inversely related to the wavelength. Comparing the stationary bulk temperature with the mean speed at each wavelength, it is possible to stablish a correlation between the temperature increase and the velocity of the particles, further supporting the relationship between the temperature and the photophoretic nature of the observed motion.

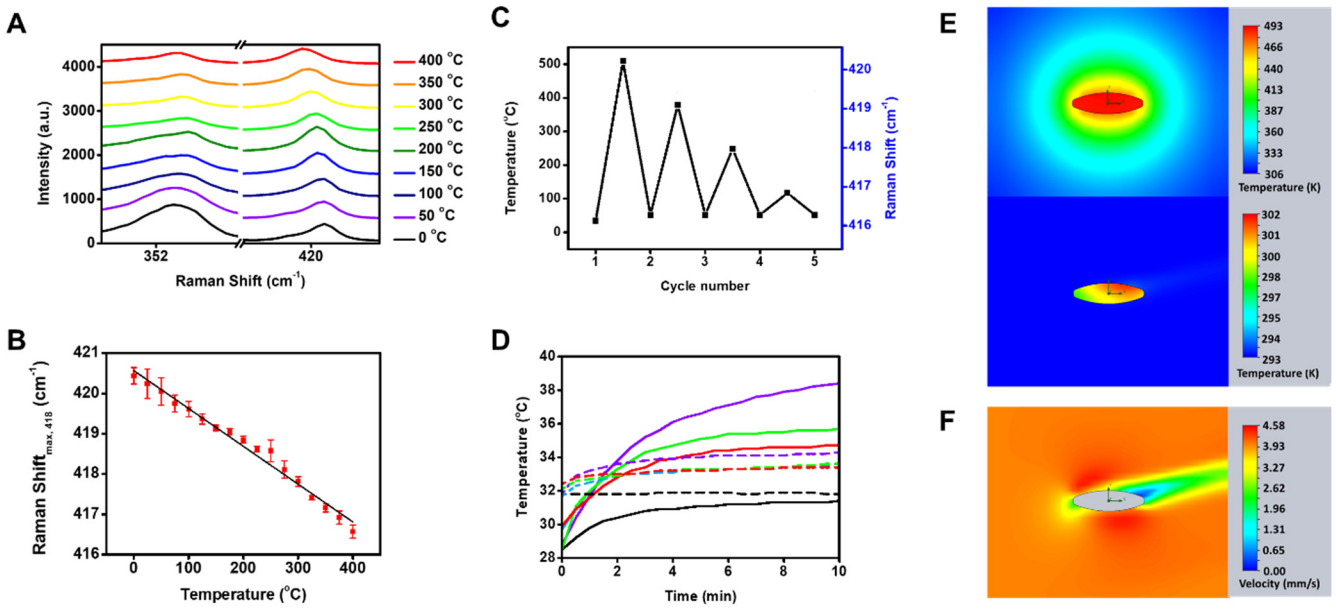

Fig 5. Effect of temperature on the micromotors: A) Raman spectra of the main bands of WS_2 micromotors at different temperatures. B) Raman shift maximum in the 418 cm^{-1} region at different temperatures, and C) Calculated temperature under external irradiation during 6 cycles and maximum Raman shift of the A_{1g} band of WS_2. D) Bulk temperature of WS_2 dispersions in water (solid lines) and water without micromotors (dashed lines) under different 385 nm (violet lines), 475 nm (blue lines), 550 nm (green lines), and 621 nm (red lines). E) Simulation of the heating of a single micromotor without (left) and with (right) flow conditions. F) Simulation of the speed flow considering the measured flow velocity.

To prove the feasibility of this propulsion mechanism in our system, a single particle was modelled using the mean particle diameter and height measured by AFM. Subsequently, a series of computational fluid dynamics (CFD) simulations were carried out using the Fluid Simulation tool embedded within the SOLIDWORKS 3D CAD software. Firstly, the energy input applied to the upper half was iteratively estimated aiming for a mean stationary local temperature of 493 K, which lies between the observed temperature interval measured by Raman spectroscopy experiments (approx. 220ºC). Next, a mean speed of 4 mm s^{-1} was applied aiming for a stationary state, the pitch angle was also estimated by matching it iteratively with the temperature distribution in the particle and maxing out the heat transfer. This optimized angle was estimated to be around 11º. This stationary state was recorded and as can be seen

in **Fig. 5E**, there is a temperature gradient across the particle, ranging from 297 K to 303 K, the surrounding water has a minimum temperature of 293 K, matching that of the environment, and a maximum temperature of 303 K. Please note that an energy input was introduced in the top part of the microparticle in all cases to simulate lighting in the y-axis. As can be observed in the results from **Fig. 5E**, this energy input induces an even heat distribution in the equilibrium. Regarding the simulation in the operational conditions, the motion angle was set so the heat exchange is maximized. To the best of our knowledge, this are the most desirable conditions as the convective currents (induced by the dissipation of heat through the solvent), responsible for the motion of the micromotors are maximized. Finally, time-dependent analyses were performed, both for the heating and cooling processes. Both processes showed a very low response time achieving the stationary state within 10 ms and 15 ms for the heating and cooling processes respectively. This fast heat exchange process agrees with the observed behaviour with a fast acceleration to the maximum speed and without a residual accumulated speed. Finally, the flow dynamics of the photophoretic micromotors were studied as can be seen in **Fig. 5F**, showing the good hydrodynamic characteristics of the micromotors. Finally, the same studies were conducted in DMF a less thermally conductive solvent as shown in **Fig. S3**. As the results indicate, being a less conductive solvent, the micromotors can dissipate less heat retaining up to 40 ^{o}C as opposed to the 30 ^{o}C in the case of water-dispersed micromotors. These results are consistent both in the bulk temperature measurements (**Fig. S3B**) and the simulation (**Fig. S3C**). Interestingly, this locally retained temperature seems to improve micromotor motion in this solvent, although further studies should be carried out to prove this correlation.

Conclusions

We have described and explored for the first time the photothermal properties of WS_2 for obtaining the highest light-induced motion to date. The one-pot process for the synthesis of the micromotors involves a single sonication step, and further modification steps can be easily performed due to the high modification capabilities of the WS_2, for example by granting them magnetic properties without hindering the motion capabilities of these micromotors. Experiments were judiciously designed to get insights into the underlying propulsion mechanism. Efficient motion in DMF media revealed the negligible influence of an electrophoretic mechanism. Thus, a photophoretic mechanism with subsequent heat release creates a thermal gradient which in turn generates hydrodynamic flow. This mechanism was identified as the main responsible one for propulsion through experimental evidence and numerical simulations. Moreover, due to the nature of the energy input, both fuel and surfactants are not needed for expanding the applicability of the micromotors in different environments. Coupling different light sources and taking advantage of the inherent properties of the TMD materials, a myriad of applications is expected to be reported in fields such as environmental remediation and biosensing with a special interest in biomedical applications.

Author Contributions

Víctor de la Asunción-Nadal: Conceptualization, Data curation, Formal analysis, Investigation, Visualization, Writing - review & editing. Daniel Rojas: Conceptualization, Formal analysis, Investigation, Writing - review & editing. Beatriz Jurado-Sánchez: Conceptualization, Formal analysis, Funding acquisition, Project administration, Resources, Supervision, Writing - original draft, Writing - review & editing. Alberto Escarpa: Conceptualization, Formal analysis, Funding acquisition, Project administration, Resources, Supervision, Writing - review & editing.

Conflicts of interest

There are no conflicts to declare.

Acknowledgements

This work was supported by the Spanish Ministry of Economy, Industry and Competitiveness [grant numbers RYC-2015-17558, co-financed by EU (B.J.S)], Grant PID2020-118154GB-I00 funded by MCIN/AEI/ 10.13039/501100011033 (A. E and B.J.S); grant TED2021-132720B-I00, funded by MCIN/AEI/10.13039/501100011033 and the European Union "NextGenerationEU"/PRTR (A. E and B.J.S); the Community of Madrid [grant numbers CM/JIN/2021-012 (B.J.S), TRANSNANOAVANSENS, S2018/NMT-4349 (A.E)] and the Universidad de Alcalá [FPI contract, Plan Propio UAH (V.A.N)]. B. J.S. and A. Escarpa acknowledge funding from DISCOVER-UAH-CM Project (Ref. REACT UE-CM2021-01), co-founded by Community of Madrid (CAM) and European Union (UE), through the European Regional Development Fund (ERDF) and supported as part of the EU's response to COVID-19 pandemic.

Phyton codes are available upon request to the corresponding authors.

Notes and references

1. Y. Yoshizumi, K. Okubo, M. Yokokawa and H. Suzuki, *Langmuir*, 2016, **32**, 9381-9388.
2. E. Karshalev, B. Esteban-Fernández de Ávila and J. Wang, *J. Am. Chem. Soc.*, 2018, **140**, 3810-3820.
3. J. Parmar, D. Vilela, K. Villa, J. Wang and S. Sánchez, *J. Am. Chem. Soc.*, 2018, **140**, 9317-9331.
4. J. Llacer-Wintle, A. Rivas-Dapena, X. Z. Chen, E. Pellicer, B. J. Nelson, J. Puigmartí-Luis and S. Pané, *Adv. Mater.*, 2021, **33**, 2102049.
5. J. Kim, C. C. Mayorga-Martinez and M. Pumera, *Chem. Eng. J.*, 2022, **446**, 137342.
6. T. Maric, S. M. Beladi-Mousavi, B. Khezri, J. Sturala, M. Z. M. Nasir, R. D. Webster, Z. K. Sofer and M. Pumera, *Small*, 2020, **16**, 1902365.
7. C. C. Mayorga-Martinez, J. G. S. Moo, B. Khezri, P. Song, A. C. Fisher, Z. Sofer and M. Pumera, *Adv. Function. Mater.*, 2016, **26**, 6662-6667.
8. M. You, C. Chen, L. Xu, F. Mou and J. Guan, *Acc. Chem. Res.*, 2018, **51**, 3006-3014.
9. K. Yuan, M. Pacheco, B. Jurado-Sánchez and A. Escarpa, *Adv. Intell. Syst.*, 2021, **3**, 2100002.

10. C. Gao, Y. Feng, D. A. Wilson, Y. Tu and F. Peng, *Small*, 2022, **15**, 2106263.
11. F. Peng, Y. Tu, J. C. M. van Hest and D. A. Wilson, *Angew. Chem. Int. Ed.*, 2015, **54**, 11662-11665.
12. H. Zhang, Z. Cao, Q. Zhang, J. Xu, S. L. J. Yun, K. Liang and Z. Gu, *Small*, 2020, **16**, 2002732.
13. K. K. Dey, S. Bhandari, D. Bandyopadhyay, S. Basu and A. Chattopadhyay, *Small*, 2013, **9**, 1916-1920.
14. K. I. Morozov and A. M. Leshansky, *Phys. Chem. Chem. Phys.*, 2020, **22**, 16407-16420.
15. F. Peng, Y. Tu, Y. Men, J. C. M. van Hest and D. A. Wilson, *Adv. Mater.*, 2017, **29**, 1604996.
16. P. S. Schattling, M. A. Ramos-Docampo, V. Salgueiriño and B. Städler, *ACS Nano*, 2017, **11**, 3973-3983.
17. D. Zhou, Y. Gao, J. Yang, Y. C. Li, G. Shao, G. Zhang, T. Li and L. Li, *Adv. Sci.*, 2018, **5**, 1800122.
18. T. Xu, Y. Luo, C. Liu, X. Zhang and S. Wang, *Anal. Chem.*, 2020, **92**, 7816-7821.
19. L. Xu, F. Mou, H. Gong, M. Luo and J. Guan, *Chem. Soc. Rev.*, 2017, **46**, 6905-6926.
20. S. Y. Tee, K. Y. Win, S. S. Goh, C. P. Teng, K. Y. Tang, M. D. Regulacio, Z. Li and E. Ye, in *Photothermal Nanomaterials*, The Royal Society of Chemistry, 2022, DOI: 10.1039/9781839165177-00001, pp. 1-32.
21. J. Zhang, A. Laskar, J. Song, O. E. Shklyaev, F. Mou, J. Guan, A. C. Balazs, and A. Sen, *ACS Nano,* 2022, DOI: 10.1021/acsnano.2c07266.
22. F. Mou, J. Zhang, Z. Wu, S. Du, Z. Zhang, L. Xu and J. Guan, *iScience*, 2019, **19**, 415-424.
23. Z. Ye, Y. Sun, H. Zhang, B. Song and B. Dong, *Nanoscale*, 2017, **9**, 18516-18522.
24. Y. Wang, C. Zhou, W. Wang, D. Xu, F. Zeng, C. Zhan, J. Gu, M. Li, W. Zhao, J. Zhang, J. Guo, H. Feng and X. Ma, *Angew. Chem. Int. Ed.*, 2018, **57**, 13110-13113.
25. M. Chen, Z. Lin, M. Xuan, X. Lin, M. Yang, L. Dai and Q. He, *Angew. Chem. Int. Ed.*, 2021, **60**, 16674-16679.
26. O. Jovanovic, *J. Quant. Spectrosc. Radiat. Transf*, 2009, **110**, 889-901.
27. N. T. Tong, *J. Coll. Interfac. Sci.*, 1975, **51**, 143-151.
28. Z. Deng, F. Mou, S. Tang, L. Xu, M. Luo and J. Guan, *Appl. Mater. Tod.*, 2018, **13**, 45-53.
29. Y. Hu, W. Liu and Y. Sun, *ACS Appl. Mater. Interfaces.*, 2020, **12**, 41495-41505.
30. K. Eshun, H. D. Xiong, S. Yu and Q. Li, *Solid-State Electron.*, 2015, **106**, 44-49.
31. H. Liu, N. Han and J. Zhao, *RSC Adv.*, 2015, **5**, 17572-17581.
32. C. Yim, M. O'Brien, N. McEvoy, S. Winters, I. Mirza, J. G. Lunney and G. S. Duesberg, *Appl. Phys. Lett.*, 2014, **104**, 103114.
33. W. S. Yun, S. Han, S. C. Hong, I. G. Kim and J. Lee, *Phys. Rev. B*, 2012, **85**, 033305.
34. W. Choi, N. Choudhary, G. H. Han, J. Park, D. Akinwande and Y. H. Lee, *Mater. Today*, 2017, **20**, 116-130.
35. L. Cheng, J. Liu, X. Gu, H. Gong, X. Shi, T. Liu, C. Wang, X. Wang, G. Liu and H. Xing, *Adv. Mater.*, 2014, **26**, 1886-1893.
36. V. de la Asunción-Nadal, B. Jurado-Sánchez, L. Vázquez and A. Escarpa, *Chem. Sci.*, 2020, **11**, 132-140.
37. Y. Sun, Y. Liu, D. Zhang, H. Zhang, J. Jiang, R. Duan, J. Xiao, J. Xing, D. Zhang and B. Dong, *ACS Appl. Mater. Interfaces*, 2019, **11**, 40533-40542.
38. X. Peng, M. Urso, M. Ussia and M. Pumera, *ACS Nano*, 2022, **16**, 7615-7625.
39. P. Mayorga-Burrezo, C. C. Mayorga-Martinez and M. Pumera, *Adv. Function. Mater.*, 2022, **32**, 2106699.
40. M. Ussia, M. Urso, K. Dolezelikova, H. Michalkova, V. Adam and M. Pumera, *Adv. Function. Mater.*, 2021, **31**, 2101178.
41. V. Sridhar, F. Podjaski, Y. Alapan, J. Kröger, L. Grunenberg, V. Kishore, B. V. Lotsch and M. Sitti, *Sci. Robot.*, 2022, **7**, eabm1421.
42. S. Fu, D. Fu, D. Xie, L. Liu, B. Chen, Y. Ye, D. A. Wilson and F. Peng, *Appl. Mater. Tod.*, 2022, **26**, 101348.
43. L. Cheng, J. Liu, X. Gu, H. Gong, X. Shi, T. Liu, C. Wang, X. Wang, G. Liu, H. Xing, W. Bu, B. Sun and Z. Liu, *Adv. Mater.*, 2014, **26**, 1886-1893.
44. A. Berkdemir, H. R. Gutiérrez, A. R. Botello-Méndez, N. Perea-López, A. L. Elías, C.-I. Chia, B. Wang, V. H. Crespi, F. López-Urías, J.-C. Charlier, H. Terrones and M. Terrones, *Sci. Rep.*, 2013, **3**, 1755.
45. G. Plechinger, S. Heydrich, J. Eroms, D. Weiss, C. Schüller and T. Korn, *Appl. Phys. Lett.*, 2012, **101**, 101906.
46. E. Shang, J. Niu, Y. Li, Y. Zhou and J. C. Crittenden, *Environ. Poll.*, 2017, **224**, 606-614.
47. W. Liu, W. Wang, X. Dong and Y. Sun, *ACS Appl. Mater. Interfaces*, 2020, **12**, 12618-12628.
48. R. K. Manna, O. E. Shklyaev, J. Kauffman, B. Tansi, A. Sen and A. C. Balazs, *ACS Appl. Mater. Interfaces*, 2019, **11**, 18004-18012.
49. J. Teiser and S. E. Dodson-Robinson, *Astron. Astrophys.*, 2013, **555**, A98.
50. A. S. Desyatnikov, V. G. Shvedov, A. V. Rode, W. Krolikowski and Y. S. Kivshar, *Opt. Express*, 2009, **17**, 8201-8211.
51. B. Dai, J. Wang, Z. Xiong, X. Zhan, W. Dai, C.-C. Li, S.-P. Feng and J. Tang, *Nat. Nanotech.*, 2016, **11**, 1087-1092.
52. H. Horvath, *KONA Powder Part. J.*, 2014, **31**, 181-199.
53. W. Yin, L. Yan, J. Yu, G. Tian, L. Zhou, X. Zheng, X. Zhang, Y. Yong, J. Li, Z. Gu and Y. Zhao, *ACS Nano*, 2014, **8**, 6922-6933.
54. S. Najmaei, Z. Liu, P. Ajayan and J. Lou, *Appl. Phys. Lett.*, 2012, **100**, 013106.
55. F. Perrozzi, S. M. Emamjomeh, V. Paolucci, G. Taglieri, L. Ottaviano and C. Cantalini, *Sens. Actuat. B. Chem.*, 2017, **243**, 812-822.